Microscopic theory of spatiotemporal multiwave mixing in broad-area semiconductor laser amplifiers

Edeltraud Gehrig* and Ortwin Hess†
Theoretical Quantum Electronics, Institute of Technical Physics, DLR, Pfaffenwaldring 38-40, D-70569 Stuttgart, Germany
(Received 11 March 1999)

We investigate the interplay of multiwave-mixing processes with the microscopically coupled spatiotemporal light field and charge carrier dynamics in broad-area semiconductor laser amplifiers. Our theoretical description is based on extended spatially resolved Maxwell-Bloch equations including on the microscopic level spatiotemporal multiwave-mixing processes. Performing a third-order expansion in terms of the microscopic carrier distribution, we include in our description both the effects of population pulsations of the total carrier density at the beat frequency and the spatiospectral interactions of the light fields leading to gain nonlinearities as well as spatial and spectral hole burning. Our simulations show that in a broad-area semiconductor laser amplifier, spatiotemporal wave-mixing processes occur in both transverse and propagation directions of the multifrequency optical beams employed in a typical excite-probe configuration. [S1050-2947(99)05312-3]

PACS number(s): 42.55.Px, 42.65.Sf, 78.20.Bh

I. INTRODUCTION

The physical effects associated with wave mixing in nonlinear optical media have been in the center of interest in recent years, both experimentally [1–6] and theoretically [7–14]. In the field of lasers, it is, in particular, the wave mixing in semiconductor optical amplifiers which offers a variety of applications in optical communication and spectroscopy and has thus attracted particularly strong attention. Most theoretical works on wave mixing in semiconductor media have been based on the assumption of a thin (in direction of light propagation) and transversely spatially homogeneous sheet of semiconductor media. Notably, many experimental configurations may very efficiently be approximated on this basis. However, this is certainly no longer the case in a broad area or tapered semiconductor laser amplifier where, indeed, dynamically migrating optical filaments as well as longitudinal self-structuring and self-pulsations may be the dominating phenomena [15,16]. Moreover, the spatiotemporal dynamics has as a consequence that the microscopic properties of the active semiconductor media and the complex macroscopic light field dynamics are intrinsically coupled [17,15,16]. A consistent theoretical description of wave-mixing processes in broad-area semiconductor laser amplifiers thus should self-consistently include this spatiotemporal interplay of microscopic and macroscopic effects and thereby automatically comprise, e.g., nonlinear spatiotemporal waveguiding, gain saturation and carrier transport. At the same time, various dissipative processes have a significant influence on these phenomena. Among those are, in particular, the spatiotemporally varying carrier-carrier and carrier-phonon relaxation and scattering. To date, however, in most theoretical descriptions those nonlinearities in the gain, index changes, and propagation are only treated within a perturbative calculation. In particular, spatial variations and counterpropagating effects are usually disregarded [18,19].

It is the aim of this work to present a theoretical and numerical description which includes on a microscopic level (spatiotemporal) wave-mixing effects as well as the transport and thermal properties of semiconductor laser amplifiers discussed in [16]. In our theory we specifically include the (counter-)light-propagation and a light-matter interaction considering all frequency components within the gain curve of the semiconductor laser amplifier. For specificity, we focus on the mixing and nonlinear interaction of a strong pump field with a detuned weaker probe beam within the active area of a broad-area semiconductor laser amplifier. We thus extend and complement our previous studies on the propagation of two picosecond pulses in the optical resonator of a diode laser amplifier [20]. In that case, the formation of a trapped pulse reminiscent of a spatial optical soliton is caused by a combination of nonlinear index changes, self-focusing, and dynamic wave-mixing effects. In concert, these effects are the reason for a modified spatiotemporal dynamics of the optical field.

In the theoretical description of a ''strong'' and direct wave-mixing process of various light field components occurring inside semiconductor lasers, a different approach is necessary. To date one generally resorts to a separation of two distinct regimes involving the extreme cases of mixing processes which are (i) slow and (ii) fast in comparison to the carrier lifetime.

In the first case, i.e., for detuning frequencies $\delta\omega < 1$ GHz, the product $\delta\omega\tau_{sp} < 1$ spatial modulations caused by a local interaction of the light fields lead to modulations in the carrier density at the beat frequency $\delta\omega$. The effects of such a wave-mixing experiment can be observed in semiconductor lasers with small mode distances produced by, e.g., an external cavity. With the modulations exceeding the GHz regime, the carrier density can no longer follow the fast dynamics due to the relatively large carrier lifetime. In the second case, with large detunings in the GHz to THz regime-

*Also at Fachbereich Physik, University of Kaiserslautern, Erwin-Schrödinger-Strasse 46, D-67663 Kaiserlautern, Germany.
†Electronic address: Ortwin.Hess@DLR.de

(where the product $\delta\omega\tau_{sp}>1$), a second class of mechanisms becomes relevant: The carrier-carrier and carrier- phonon-scattering processes occurring on a comparatively fast time scale in the order of several hundred femtoseconds within the bands of the semiconductor can respond to the beat frequency generated by the interplay of the waves. This modulation of the distribution of electrons and holes over the different energy states of the bands can be observed, e.g., in short cavity semiconductor lasers with large frequency differences between the modes.

In the case of wide transverse-section lasers such as the broad-area laser, however, both types of regimes and, in particular, the intermediate regime between the two extremes may be relevant. It thus becomes necessary to include both the modulation of the spatiospectrally dependent intraband dynamics of the carrier distributions and the modulation of the macroscopic spatiotemporally varying carrier density. To circumvent the usual artificial separation into the two regimes, we perform a direct expansion of the microscopic Wigner distributions of electrons and holes as well as the interband polarization in terms of the unperturbed carrier distribution. This allows us to apply our wave-mixing theory in the whole range from 50 fsec to 5 nsec. Thereby the modal interactions due to the slow population pulsations (nanosecond regime) at the beat frequency of the participating beams on the one hand and the spatial and spectral interactions leading to gain nonlinearities and mode competition via spatial and spectral hole burning on a picosecond time scale on the other hand are simultaneously and self-consistently captured by our theory. It is then via the dynamically varying interband polarizations that these microscopic coupling mechanisms are dynamically transformed to the wave mixing of the light fields.

In this work, we will specifically investigate the spatiospectral wave-mixing processes in a broad-area semiconductor laser amplifier into which a strong pump beam and a weaker probe beam having a different frequency are injected. In Sec. II we will present and discuss the theoretical model which is the basis for the numerical results presented in Sec. III. Section IV concludes the paper.

II. MULTIWAVE MAXWELL-BLOCH EQUATIONS FOR SPATIALLY INHOMOGENEOUS SEMICONDUCTOR LASERS

In the following, we present a theoretical description of the microscopic multiwave spatiotemporal dynamics of spatially inhomogeneous semiconductor lasers. For specificity, we will concentrate on typical III-V semiconductor material systems, i.e., choosing the relevant parameters for the GaAs-$Al_xGa_{1-x}As$ system. Although we will focus here on a simple setup involving an inverted semiconductor laser amplifier with injection of a strong pump wave and a weaker probe wave, a generalization to the description of a more complex situation involving the interaction of a multitude of coexisting optical fields in the active area will be straightforward.

The microscopic dynamics of the carrier distributions of electrons (e) and holes (h) $f^{e,h}(k,\mathbf{r},t)$ and the interband polarization is governed by the semiconductor Bloch equations [16]:

$$\begin{aligned}\frac{\partial}{\partial t}f^{e,h}(k,\mathbf{r},t)&=g(k,\mathbf{r},t)-\gamma_{e,h}(k,N)\\&\quad\times[f^{e,h}(k,\mathbf{r},t)-f^{e,h}_{eq}(k,\mathbf{r},t)]\\&\quad-\gamma^{\mathrm{LO}}_{e,h}(k,N)[f^{e,h}(k,\mathbf{r},t)-f^{e,h}_{eq,l}(k,\mathbf{r},t)]\\&\quad+\Lambda^{e,h}(k,\mathbf{r},t)-\Gamma_{sp}(k,\mathbf{r})f^{e}(k,\mathbf{r},t)f^{h}(k,\mathbf{r},t)\\&\quad-\gamma_{nr}f^{e,h}(k,\mathbf{r},t),\end{aligned}\tag{1}$$

$$\begin{aligned}\frac{\partial}{\partial t}p^{\pm}_{\mathrm{nl}}(k,\mathbf{r},t)&=-[i\overline{\omega}(k)+\tau_p^{-1}(k,N)]p^{\pm}(k,\mathbf{r},t)\\&\quad+\frac{1}{i\hbar}d_{cv}(k)E^{\pm}(\mathbf{r},t)[f^{e}(k,\mathbf{r},t)+f^{h}(k,\mathbf{r},t)]\end{aligned}$$

with

$$\begin{aligned}g(k,\mathbf{r},t)&=-\frac{1}{4i\hbar}d_{cv}(k)[E^{+}(\mathbf{r},t)p^{+}{}^{*}(k,\mathbf{r},t)\\&\quad+E^{-}(\mathbf{r},t)p^{-}{}^{*}(k,\mathbf{r},t)]+\frac{1}{4i\hbar}d^{*}_{cv}(k)\\&\quad\times[E^{+}{}^{*}(\mathbf{r},t)p^{+}(k,\mathbf{r},t)+E^{-}{}^{*}(\mathbf{r},t)p^{-}(k,\mathbf{r},t)].\end{aligned}\tag{2}$$

Thereby the interband polarization consists of a linear, $p_l(k,\mathbf{r},t)$, and a nonlinear part, $p_{\mathrm{nl}}(k,\mathbf{r},t)$, where the linear part is given by

$$p_l(k,\mathbf{r},t)=\frac{d_{cv}(k)}{\hbar}\frac{1}{\overline{\omega}(k)-i\tau_p^{-1}(k)}E^{\pm}(\mathbf{r},t).\tag{3}$$

In Eq. (1), k denotes the carrier-momentum wave number; $\mathbf{r}=(x,z)$ represents the lateral and longitudinal direction, respectively. $f^{e,h}_{\mathrm{eq}}(k,\mathbf{r},t)$ is the carrier distribution in thermal equilibrium within the electron-hole plasma, $f^{e,h}_{\mathrm{eq},l}(k,\mathbf{r},t)$ is the carrier distribution in thermal equilibrium with the lattice given by the corresponding Fermi function, and $E^{\pm}(\mathbf{r},t)$ are the counterpropagating optical fields in the active area. The relaxation rates of spontaneous emission, $\Gamma_{\mathrm{sp}}(k,\mathbf{r})$, nonradiative recombination, γ_{nr}, the microscopically calculated rates $\gamma_{e,h}(k,N(\mathbf{r}),t)$ for the carrier-carrier scattering processes and $\gamma^{LO}_{e,h}(k,N(\mathbf{r}),t)$ for the carrier-(longitudinal-optical) phonon scattering [17], and $\tau_p^{-1}(k,N(\mathbf{r}),t)=[\gamma_e(k,N(\mathbf{r}),t)+\gamma_h(k,N(\mathbf{r}),t)]$ as well as the frequency detuning $\overline{\omega}(k,T_l)$ between the cavity frequency ω and the transition frequency pertain to the optical probe field. e,h is the microscopic pump term and d_{cv} is the optical dipole matrix element [16].

In order to describe a particular experimental setup, in which a strong optical pump field (wave number k_0) and one or two additional weak beams (e.g., a probe beam, with wave number $k_1=k_0+\Delta k$, and the generated conjugate signal with wave number $k_2=k_0-\Delta k$) are counterpropagating

within the active layer of a semiconductor laser, the total optical field is partitioned according to

$$\mathbf{E}^{\pm}(\mathbf{r},t)=E_0^{\pm}(\mathbf{r},t)+E_1^{\pm}(\mathbf{r},t)e^{i\delta\omega t}+E_2^{\pm}(\mathbf{r},t)e^{-i\delta\omega t}. \tag{4}$$

To derive equations describing the response of the carriers to the interaction of the various light fields, we use an analog expansion for the Wigner distributions of the carriers and the interband polarization:

$$\begin{aligned} f^{e,h}&=f_0(k,\mathbf{r},t)+f_1^{e,h}(k,\mathbf{r},t)e^{i\delta\omega t}+f_2^{e,h}(k,\mathbf{r},t)e^{-i\delta\omega t},\\ p_{\mathrm{nl}}&=p_{\mathrm{nl}_0}(k,\mathbf{r},t)+p_{\mathrm{nl}_1}(k,\mathbf{r},t)e^{i\delta\omega t}+p_{\mathrm{nl}_2}(k,\mathbf{r},t)e^{-i\delta\omega t}. \end{aligned} \tag{5}$$

Thereby $f_0(k,\mathbf{r},t)$ and $p_{\mathrm{nl}_0}(k,\mathbf{r},t)$ denote the carrier distribution and the interband polarization, respectively, in the absence of the additional fields, E_1 and E_2, and $\delta\omega=\omega_1-\omega_0=\omega_0-\omega_2$ is the detuning between pump E_0 (at frequency ω_0) and probe field. Note that it is the fact that these expansions are performed on the microscopic level which—via the microscopic dynamics of the carrier distributions and the interband polarization—will automatically lead to a self-consistent inclusion of the mixing and interaction of the optical fields as well as the modulation and response of the carriers to the light field dynamics. Inserting Eq. (4) into Eq. (1) leads to the following expression for the spatiospectral dynamics of the total carrier distribution:

$$\begin{aligned} &\frac{\partial}{\partial t}[f_0^{e,h}(k,\mathbf{r},t)+f_1^{e,h}(k,\mathbf{r},t)e^{i\delta\omega t}+f_2^{e,h}(k,\mathbf{r},t)e^{-i\delta\omega t}]\\ &=-\frac{1}{4i\hbar}d_{cv}\{[E_0^+(\mathbf{r},t)+E_1^+(\mathbf{r},t)e^{i\delta\omega t}+E_2^+(\mathbf{r},t)e^{-i\delta\omega t}][p_0^{+*}(k,\mathbf{r},t)+p_1^{+*}(k,\mathbf{r},t)e^{-i\delta\omega t}+p_2^{+*}(k,\mathbf{r},t)e^{i\delta\omega t}]\\ &\quad+[E_0^-(\mathbf{r},t)+E_1^-(\mathbf{r},t)e^{i\delta\omega t}+E_2^-(\mathbf{r},t)e^{-i\delta\omega t}][p_0^{-*}(k,\mathbf{r},t)+p_1^{-*}(k,\mathbf{r},t)e^{-i\delta\omega t}+p_2^{-*}(k,\mathbf{r},t)e^{i\delta\omega t}]\}\\ &\quad+\frac{1}{4i\hbar}d_{cv}\{[E_0^{+*}(\mathbf{r},t)+E_1^{+*}(\mathbf{r},t)e^{-i\delta\omega t}+E_2^{+*}(\mathbf{r},t)e^{i\delta\omega t}][p_0^{+}(k,\mathbf{r},t)+p_1^{+}(k,\mathbf{r},t)e^{i\delta\omega t}+p_2^{+}(k,\mathbf{r},t)e^{-i\delta\omega t}]\\ &\quad+[E_0^{-*}(\mathbf{r},t)+E_1^{-*}(\mathbf{r},t)e^{-i\delta\omega t}+E_2^{-*}(\mathbf{r},t)e^{i\delta\omega t}][p_0^{-}(k,\mathbf{r},t)+p_1^{-}(k,\mathbf{r},t)e^{i\delta\omega t}+p_2^{-}(k,\mathbf{r},t)e^{-i\delta\omega t}]\}\\ &\quad-\gamma_{e,h}(k,N)[f_0^{e,h}(k,\mathbf{r},t)+f_1^{e,h}(k,\mathbf{r},t)e^{i\delta\omega t}+f_2^{e,h}(k,\mathbf{r},t)e^{-i\delta\omega t}-f_{\mathrm{eq}}^{e,h}(k,\mathbf{r},t)]+\Lambda^{e,h}(k,\mathbf{r},t)-\Gamma_{\mathrm{sp}}(k,\mathbf{r})[f_0^{e}(k,\mathbf{r},t)\\ &\quad+f_1^{e}(k,\mathbf{r},t)e^{i\delta\omega t}+f_2^{e,h}(k,\mathbf{r},t)e^{-i\delta\omega t}][f_0^{h}(k,\mathbf{r},t)+f_1^{h}(k,\mathbf{r},t)e^{i\delta\omega t}+f_2^{e,h}(k,\mathbf{r},t)e^{-i\delta\omega t}]\\ &\quad-\overline{\gamma}_{\mathrm{nr}}[f_0^{e,h}(k,\mathbf{r},t)+f_1^{e,h}(k,\mathbf{r},t)e^{i\delta\omega t}+f_2^{e,h}(k,\mathbf{r},t)e^{\delta\omega t}]. \end{aligned} \tag{6}$$

Finally we obtain to second order the following equations for the time-dependent light-field driven carrier dynamics (for notational simplicity, the k, $\mathbf{r}$, and t dependence have been omitted):

$$\begin{aligned} \frac{\partial}{\partial t}f_1^{e,h}&=-\frac{1}{4i\hbar}d_{cv}[(E_1^+p_0^{+*}+E_0^+p_2^{+*}-E_1^{+*}p_0^+-E_0^{+*}p_2^+)\\ &\quad+(E_1^-p_0^{-*}+E_0^-p_2^{-*}-E_1^{-*}p_0^--E_0^{-*}p_2^-)]\\ &\quad-\Gamma_{ges}^{e,h}f_1^{e,h},\\ \frac{\partial}{\partial t}f_2^{e,h}&=-\frac{1}{4i\hbar}d_{cv}[(E_0^+p_1^{+*}+E_2^+p_0^{+*}-E_0^{+*}p_1^+-E_2^{+*}p_0^+)\\ &\quad+(E_0^-p_1^{-*}+E_2^+p_0^{+*}-E_0^{-*}p_1^-+E_2^{+*}p_0^+)]\\ &\quad-\Gamma_{ges}^{e,h}f_2^{e,h}, \end{aligned} \tag{7}$$

where we have approximated the spontaneous emission rate with

$$\Gamma_{\mathrm{sp}}(f_0^ef_{1,2}^h+f_{1,2}^ef_0^h)\approx\Gamma_{\mathrm{sp}}f_0^{h,e}f_{1,2}^{e,h}. \tag{8}$$

Integration of Eq. (7) assuming only slowly varying field amplitudes leads to

$$\begin{aligned} f_1^{e,h}&=\frac{1}{i\delta\omega+\Gamma_{ges}^{e,h}}\left(-\frac{1}{4i\hbar}\right)[(E_1^+p_0^{+*}+E_0^+p_2^{+*}-E_1^{+*}p_0^+\\ &\quad+E_0^{+*}p_2^+)+(E_1^-p_0^{-*}+E_0^-p_2^{-*}-E_1^{-*}p_0^-\\ &\quad-E_0^{-*}p_2^-)],\\ f_2^{e,h}&=\frac{1}{-i\delta\omega+\Gamma_{ges}^{e,h}}\left(-\frac{1}{4i\hbar}\right)[(E_0^+p_1^{+*}+E_2^+p_0^{+*}-E_0^{+*}p_1^+\\ &\quad-E_2^{+*}p_0^+)+(E_0^-p_1^{-*}+E_2^-p_0^{-*}-E_0^{-*}p_1^-\\ &\quad-E_2^{-*}p_0^-)], \end{aligned} \tag{9}$$

with

$$\Gamma_{ges}^{e,h}=\gamma_{e,h}+\gamma_{\mathrm{nr}}+\Gamma_{\mathrm{sp}}f^{h,e}. \tag{10}$$

Equation (9) describes the changes in the carrier density originating from the additional light fields, E_1 and E_2, and their interaction with the main field, E_0.

TABLE I. Fundamental material and device parameters of the broad-area ($GaAs/Al_xGa_{1-x}As$) semiconductor lasers.

L (cavity length)	750 μm
d (thickness of active layer)	0.15 μm
n_c [refr. index of the cladding layers ($Ga_xAl_{1-x}As$)]	3.35
n_l [refr. index of active layer (GaAs)]	3.59
λ (laser wavelength)	815 nm
R_1 (front facet mirror reflectivity)	10^{-4}
R_2 (back facet mirror reflectivity)	10^{-4}
τ_{nr} (nonrad. recombination time)	5 ns
a_0 (exciton Bohr radius)	1.243×10^{-6} cm
m_0 (mass of the electron)	9.1093879×10^{-31} kg
m_e (effective electron mass)	$0.067m_0$
m_h (effective hole mass)	$0.246m_0$
$\mathcal{E}_g(0)$ (semiconductor energy gap at $T=0$ K)	1.519 eV
D_p (diffraction coefficient)	18×10^{-6} m
η_i (injection efficiency)	0.5
Γ (confinement factor)	0.55/0.54
α_w (absorption)	30 cm^{-1}
v_{sr} (surface recombination velocity)	10^6 m/s

The expressions for the total carrier distribution functions, $f^{e,h}=f_1^{e,h}e^{i\delta\omega t}+f_2^{e,h}e^{-i\delta\omega t}$, can now be introduced into the equation for the nonlinear part of the microscopic interband polarization:

$$\begin{aligned}\frac{\partial}{\partial t}&(p^{\pm}_{\mathrm{nl}_0}+p^{\pm}_{\mathrm{nl}_1}e^{i\delta\omega t}+p^{\pm}_{\mathrm{nl}_2}e^{-i\delta\omega t})\\&=-[i\overline{\omega}+\tau_p^{-1}](p^{\pm}_{\mathrm{nl}_0}+p^{\pm}_{\mathrm{nl}_1}e^{i\delta\omega t}+p^{\pm}_{\mathrm{nl}_2}e^{-i\delta\omega t})\\&\quad+\frac{1}{i\hbar}d_{cv}(E_0^{\pm}+E_1^{\pm}e^{i\delta\omega t}+E_2^{\pm}e^{-i\delta\omega t})[f_0^e+f_1^e e^{i\delta\omega t}\\&\quad+f_2^e e^{-i\delta\omega t}+f_0^h+f_1^h e^{i\delta\omega t}+f_2^h e^{-i\delta\omega t}].\end{aligned}\tag{11}$$

An analytical expression for the coefficients $p^{\pm}_{\mathrm{nl}_1}$ and $p^{\pm}_{\mathrm{nl}_2}$ can be obtained by considering Eq. [11] in adiabatic elimination,

$$\begin{aligned}p_{\mathrm{nl}_1}&=-\frac{d_{cv}}{\hbar}\frac{1}{\overline{\omega}_1-i\tau_p}[(f_0^e+f_0^h)E_1+(f_1^e+f_1^h)E_0],\\p_{\mathrm{nl}_2}&=-\frac{d_{cv}}{\hbar}\frac{1}{\overline{\omega}_2-i\tau_p}[(f_0^e+f_0^h)E_2+(f_2^e+f_2^h)E_0],\end{aligned}\tag{12}$$

which can be inserted in the full dynamical equation [11] for the total interband polarization. The macroscopic polarizations, which are related to the three optical fields, are given by the summation over the respective interband polarizations,

$$P_i(\mathbf{r},t)=\frac{2}{\mathcal{V}}\sum_k d_{cv}p_i(k,\mathbf{r},t),\tag{13}$$

where $\mathcal{V}$ is the volume of the active layer. They enter the wave equations which describe the spatiotemporal dynamics of the counterpropagating optical fields (c.f. [16]):

$$\begin{aligned}&\pm\frac{\partial}{\partial z}E^{\pm}_{0,1,2}(\mathbf{r},t)+\frac{n_l}{c}\frac{\partial}{\partial t}E^{\pm}_{0,1,2}(\mathbf{r},t)\\&\quad=\frac{i}{2}\frac{1}{K_z(\lambda)}\frac{\partial^2}{\partial x^2}E^{\pm}_{0,1,2}(\mathbf{r},t)-\left(\frac{\alpha}{2}+i\Delta\right)E^{\pm}_{0,1,2}(\mathbf{r},t)\\&\quad\quad+\frac{i}{2}\frac{\Gamma}{n_l^2\epsilon_0 L}P^{\pm}_{0,1,2}(\mathbf{r},t).\end{aligned}\tag{14}$$

$K_z(\lambda)$ contains the wavelength dependence of the wave number K_z, α denotes the linear absorption coefficient, and Δ models the passive waveguiding structure of the cavity. The spatiotemporal varying carrier density is at every location given by

$$N(\mathbf{r},t)=\sum_k f^{e,h}(k,\mathbf{r},t)\tag{15}$$

and thus includes every modulation and response of the carriers, i.e., the interband dynamics without change in total density and also the density modulation via the slow interband dynamics, each with their respective time scale. The material and structural parameters of the broad-area semiconductor lasers amplifiers are summarized in Table I.

The set of equations, Eq. (1) with Eq. (9) together with Eqs. (14) and (15), is the basis for our numerical simulation and in the following will be applied to model typical pump-probe situations. Additionally, the spatiotemporal temperature-related dynamics of the nonequilibrium carrier distributions is considered on the basis of hydrodynamic equations derived from the Boltzmann equation [16]. Specifically, we analyze the situation schematically depicted in Fig. 1, where a strong pump beam at frequency ω_0 and a positively ($\omega_1=\omega_0+\delta\omega$) or negatively ($\omega_2=\omega_0-\delta\omega$) detuned weak probe beam are injected into a broad-area amplifier. The consideration of the spatial dependence of all variables generally allows modeling arbitrary injection angles

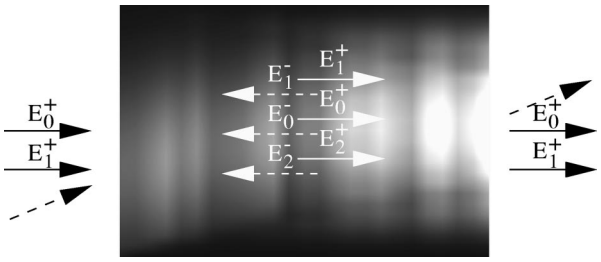

FIG. 1. Scheme of the wave-mixing setup: a strong pump beam and a weak probe beam of different frequency are optically injected into a broad-area semiconductor laser amplifier.

and beam profiles. As examples, we will pick the following cases: parallel injection of both beams with small ($\delta\omega\tau_{sp}<1$) and strong ($\delta\omega\tau_{sp}>1$) negative detuning, parallel injection with small positive detuning, as well as the situation of a weakly negatively detuned probe beam at oblique incidence.

III. SPATIOSPECTRAL WAVE MIXING IN BROAD-AREA LASERS

Figure 1 illustrates the typical wave-mixing configuration in a broad-area semiconductor laser amplifier (here with length $L=750$ μm, width $w=100$ μm, and central wavelength of $\lambda=815$ nm): A strong pump field E_0 (here considered as a Gaussian beam with a full width at half maximum of 50 μm and total power of 5 mW) whose central frequency ω_0 lies within the gain curve of the (antireflectivity-coated) semiconductor laser amplifier is injected from one side. Next to the forward-propagating wave (i.e., in the direction of the injection), a counterpropagating wave of equal frequency is excited by the interaction of the light field with the active medium: The spatiospectral carrier dynamics leads to spatially varying density distributions which via the induced refractive index act as a diffraction grating for the forward-propagating wave. The immediate response of the active medium to the incoming wave is thus a backward traveling wave which from there on coexists with the former. Even though the second wave is in comparison to the forward-propagating wave of considerably lower intensity, its existence is important for the spatiotemporal behavior of the device—in particular in a wave-mixing situation which due to the microscopic coupling of the light fields reacts rather sensitively to spatiospectral variations.

The second light beam injected into the laser, marked E_1 in Fig. 1, is a probe beam of relatively low intensity (5 μW) at frequency $\omega_0-\delta\omega$ ($\delta\omega$ being the pump-probe detuning) which may be injected in parallel to the pump beam or with oblique incidence. The nonlinear interaction between the pump field and the probe field (which also consists of forward and backward traveling field contributions) and in particular their microscopic coupling via the active medium creates a third wave at $\omega_0+\delta\omega$. Depending on the beam and material characteristics, geometrical configuration, as well as frequency detuning, the three optical waves can spatiotemporally develop quite differently.

The microscopic approach discussed above allows in principal an analysis of small frequency detunings (MHz regime) as well as large detunings (GHz regime), since the physical mechanisms responsible for the energy transfer in each frequency and corresponding time regime are each considered with their respective time scale. These are, in particular, the fast intraband carrier-carrier and carrier-phonon scattering processes in the case of small frequency detunings and the slow population pulsations of the carrier density in the case of the large detuning. With the spatial transport of charge carriers occurring on a picosecond (10 ps, . . . ,5 ns) time scale and the energy transfer via various carrier-phonon scattering processes also spanning the whole time regime from picoseconds to nanoseconds, it is thus important to consider all these effects in their full spatiospectral dependence and, in particular, their coupling in the microscopic and macroscopic domain.

In the following we will discuss two representative examples with frequency detunings of 100 MHz and 3 GHz, and compare the parallel beam propagation with the configuration involving a probe beam which is injected at an angle of 25°. In addition, we will visualize the difference between the low- and high-frequency injection of the probe beam with respect to the pump beam arising from band structure and carrier occupation effects. Since the microscopic distributions give more complete information and a better insight into the spatiospectral interactions than the macroscopic fields (such as intensity or density), we will in the following particularly use the microscopic Wigner distributions of the electrons and the interband polarization in our discussion of the spatiotemporal wave-mixing situation.

For the case of two beams propagating in parallel, Figs. 2–5 display snapshots of the nonequilibrium Wigner distributions of the electrons $\delta f^e=f^e(k,x=w/2,z,t_i)-f^e_{eq}(k,x=w/2,z,t_i)$ as well as the real and imaginary parts of the nonlinear interband polarization, $p'_{nl}=p'_{nl}(k,x=w/2,z,t_i)$ and $p''_{nl}=p''_{nl}(k,x=w/2,z,t_i)$, respectively. Note that for reasons of visualization only their dependence on the longitudinal (z) direction, i.e., the direction of propagation, is displayed, while the full space dependence $\mathbf{r}=(x,z)$ is considered in the simulations. In the case of oblique incidence, we will show the transverse dependence (Fig. 6) at three longitudinal positions $p'_{nl}=p'_{nl}(k,x,z=0,L/2,L)$ and $p''_{nl}=p''_{nl}(k,x,z=0,L/2,L)$ (front facet, middle, back facet) while the longitudinal distributions in our example are qualitatively very similar to the case of the parallel propagation (since for injection of the probe beam at a lateral position near the pump beam and the rather large lateral extension of the beams, both lead to a permanent spatiospectral overlap of the light fields).

A. Spatiospectral holeburning

The nonequilibrium Wigner distribution of the electrons is visualized in Fig. 2 in dependence on the propagation direction (z) and frequency (in units of the exciton-Bohr radius $a_0=1.295\times10^{-6}$ cm) for a frequency detuning of 100 MHz and an injected probe beam (5 mW) at $\omega_0=2\pi c/\lambda_0$ with $\lambda_0=815$ nm and a probe beam at $\omega=\omega_0-\delta\omega$(5 μW). The unperturbed contribution displayed in Fig. 2(a) shows the typical spatiospectral hole—representing local stimulated coherent emission—which during propagation of the pump beam spectrally broadens. At the same time, carriers are accumulated by the carrier-phonon coupling at neighboring fre-

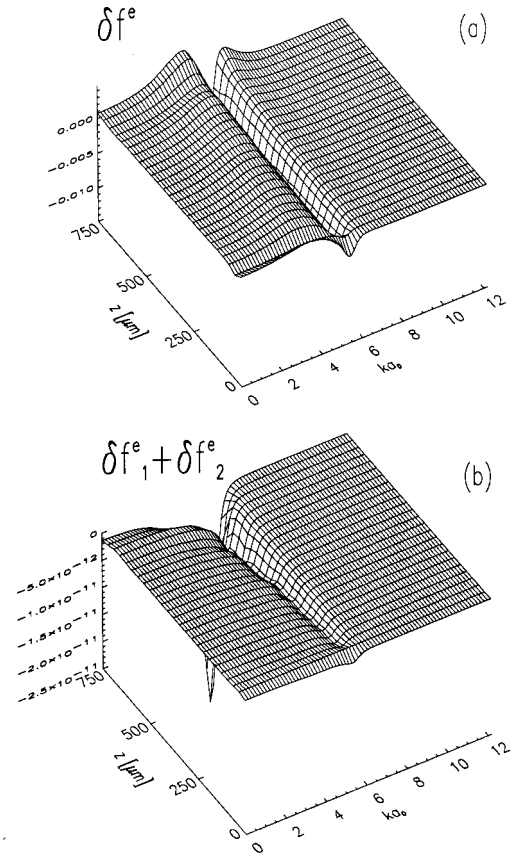

FIG. 2. Wigner distribution of the electrons $f^e(k,z,t) - f^e_{\rm eq}(k,z,t)$ (a), and sum of the contributions $f^e_1(k,z,t)$ and $f^e_2(k,z,t)$ in the case of parallel injection of the pump beam (5 mW) and the probe beam (5 μW) of lower frequency, respectively. The frequency detuning is 100 MHz.

quencies leading to energy transfer in the frequency domain. Figure 2(b) displays the sum of the changes created by the propagation and interaction of the three optical fields E_0, E_1, and E_2 in the Wigner distribution of the electrons. Due to the relatively small detuning, their contributions spatiospectrally overlap close to the central frequency ω_0 forming a spatiospectral trench which adds to the unperturbed distribution of Fig. 2(a). Due to the different amplitudes of E_0, E_1, and E_2, this trench appears spectrally slightly asymmetric.

With the complex interband polarization $p_{\rm nl}$ being directly related to the microscopic susceptibility, its real and imaginary parts can be used to visualize the combined spatial and spectral changes in the microscopic generation rate and in the carrier-induced refractive index. The complex interband polarization $p_{\rm nl}$ thus contains information on the dynamic variation of the spatiospectral distribution of both the gain and the refractive index.

B. Small detuning

The left column of Fig. 3 displays the contributions of the real part of the nonlinear polarization belonging (a) to the pump field E_0, $p'_{\rm nl}$ at ω_0, (b) to the probe field, $p'_{\rm nl1}$ at $\omega_0 - \delta\omega$, and (c) the conjugate contribution, $p'_{\rm nl2}$ at $\omega_0 + \delta\omega$, which has been created via the interaction of pump and probe beams in the medium. They visualize the dependence of the fields on propagation (z axis) and on frequency (scaled in multiples of the exciton-Bohr radius $a_0 = 1.295 \times 10^{-6}$ cm). In Fig. 3 the frequency detuning between the pump and probe wave is 100 MHz. The right column of Fig. 3 displays the respective imaginary contributions in the polarization. The real part of the pump and probe contribution, Figs. 3(a) and 3(b), respectively, shows the formation of a spatiospectral trench which increases in the propagation direction. This can be understood on the basis of carrier-induced changes in the nonlinear frequency-dependent refractive index which increase during propagation. The distributions show distinct changes in sign in both frequency and space domain. With the real part of the polarization being related to the inverse of the carrier-induced refractive index, one can detect a typical dispersion form. The rather moderate injection current leads during propagation to a transition from absorption to gain, visualized by the change in sign. The imaginary part displayed in Fig. 3 for the pump (d) and the probe wave (e) can be understood as a spatiospectral gain distribution. The positive values at the front facet ($z=0$) reveal absorption, which is the cause of an accumulation of heated carriers at high-frequency values. The change towards negative values during the propagation, on the other hand, visualizes the carrier depletion near the band gap being related to gain. Since the amplifier current was only slightly above the threshold value, the polarization in the absorption and gain regime is of similar magnitude. The pump-probe detuning is rather small compared to typical amplifier gain curves, which are spectrally rather broad ($\approx$50 nm). Thus, the spectrally dependent gain and index changes affecting the pump and the probe wave are qualitatively the same. The respective trenches which are formed in the interband polarization distributions thus are also of similar shape. For higher amplifier currents, the carrier depletion caused by the two modes and their interaction leads to a higher gain for the main field and a damping of the second injected field.

The modulation of the interband carrier dynamics at the beat frequency $\delta\omega$ of the pump and the probe wave now leads to the formation of an optical field at $\omega + \delta\omega$, which can be seen in Figs. 3(c) and 3(f) for the real and imaginary parts of the interband polarization, respectively. The transfer of carriers and energy occurs due the carrier-carrier and carrier-phonon interactions in the space and frequency domain. They happen on a psec to μsec time scale and can thus respond to the interaction and beating of the light fields. Since the amplitude of this third field is very weak, the overall gain is more strongly reduced by the pump and probe field so that the amplitude of the conjugated wave E_2 is reduced.

If the injection of the probe beam occurs on the high-frequency side of the pump beam, as displayed in Figs. 4(a)–4(f), we see a qualitatively similar behavior. Thus the carrier and energy transfer in space and frequency domain can in principle occur towards higher as well as lower energy values. However, the corresponding density of states in the valence and conduction bands as well as the occupation of the bands described by the semiconductor Bloch equations lead to an asymmetry in distributions of the gain and the induced refractive index caused by an asymmetric transfer of carriers

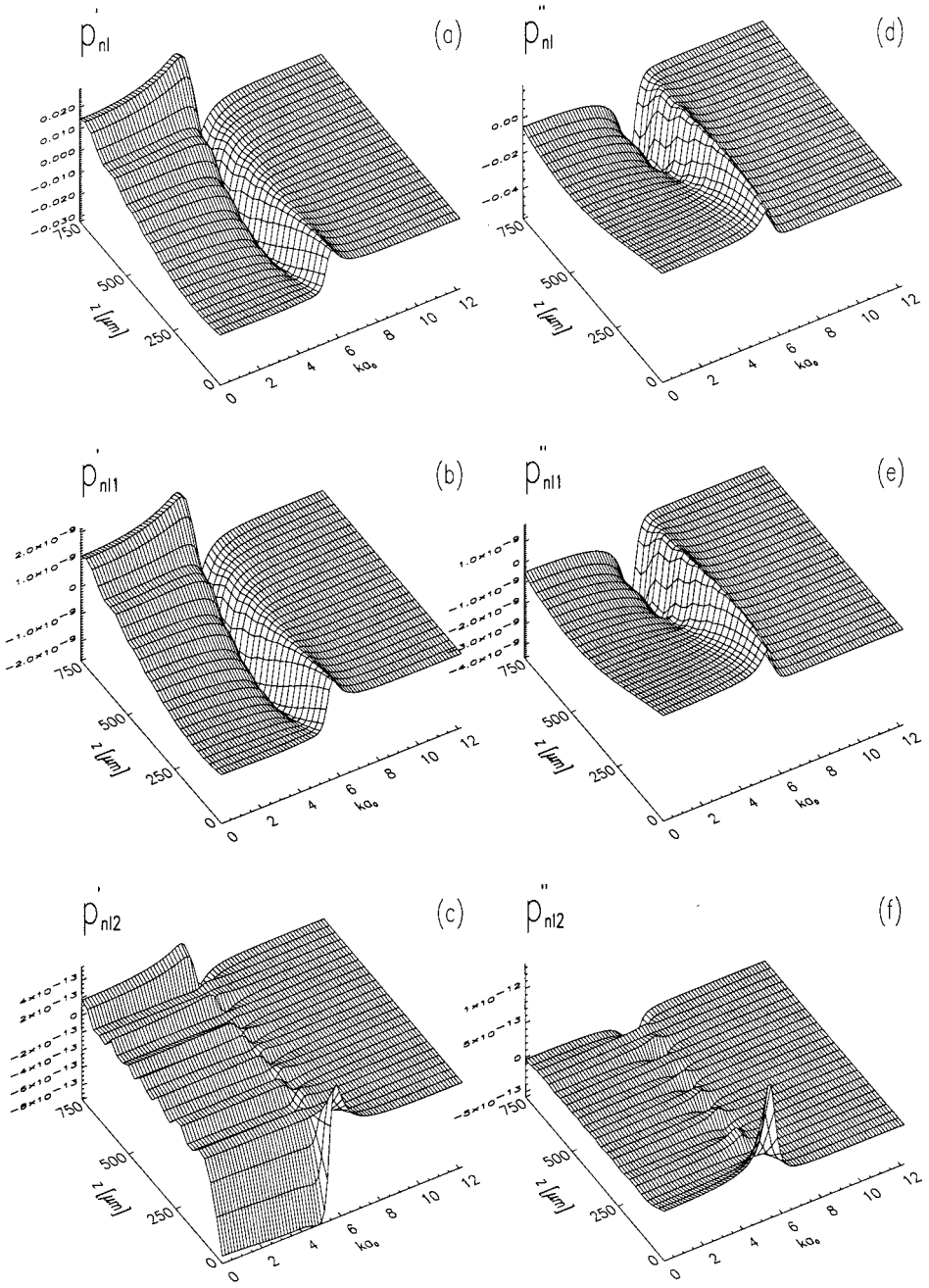

FIG. 3. Wigner distribution of the real part of the nonlinear interband polarization $p'_{\mathrm{nl}}(k,z,t)$ (left column) and the imaginary part of the nonlinear interband polarization $p''_{\mathrm{nl}}(k,z,t)$ (right column) for the situation of parallel injection of a pump beam (5 mW) and a probe beam (5 μW) of lower frequency. The frequency detuning is 100 MHz.

and energy. Comparing the amplitude of p_{nl_1} in Fig. 4(b) with the amplitude of p_{nl_2} in Fig. 3(c), one can verify that, indeed, this asymmetry leads to an increased amplitude in p_{nl_1} for the transfer from E_2 with $\omega=\omega+\delta\omega$ to E_1 with $\omega=\omega-\delta\omega$, i.e., from higher towards lower frequencies.

C. Large detuning

At first glance, the distribution of the real [Figs. 5(a)–5(c)] and imaginary parts [Figs. 5(d)–5(f)] of the nonlinear interband polarization in the situation of strong detuning exhibits a very similar behavior to the case of small detuning discussed above (Fig. 3). However, since the spectral displacement of the resonant frequencies of the three waves has changed, the overall gain and refractive index change of the waves is altered. The wide distance in frequency domain leads to a decrease in the efficiency of the light-field–matter interaction [see Eq. (13)] and thus to a weaker coupling in comparison to the situation of the small detuning discussed above. Thus the spectrally dependent carrier inversion and gain of the injected probe beam is less reduced by the influence of the pump beam (i.e., its finite phase relaxation and spectral carrier depletion and the resulting carrier relaxation and scattering), and the amplitude of the real part and the imaginary part of the nonlinear interband polarization is higher than in the case of the small detuning, although the injected power is the same (5 μW). In addition, a small frequency drift can be observed during the propagation of the probe beam. It is caused by the nonlinear interaction of these two beams, which increases during propagation due to the increased power. The polarization p_{nl_2} of the conjugate wave

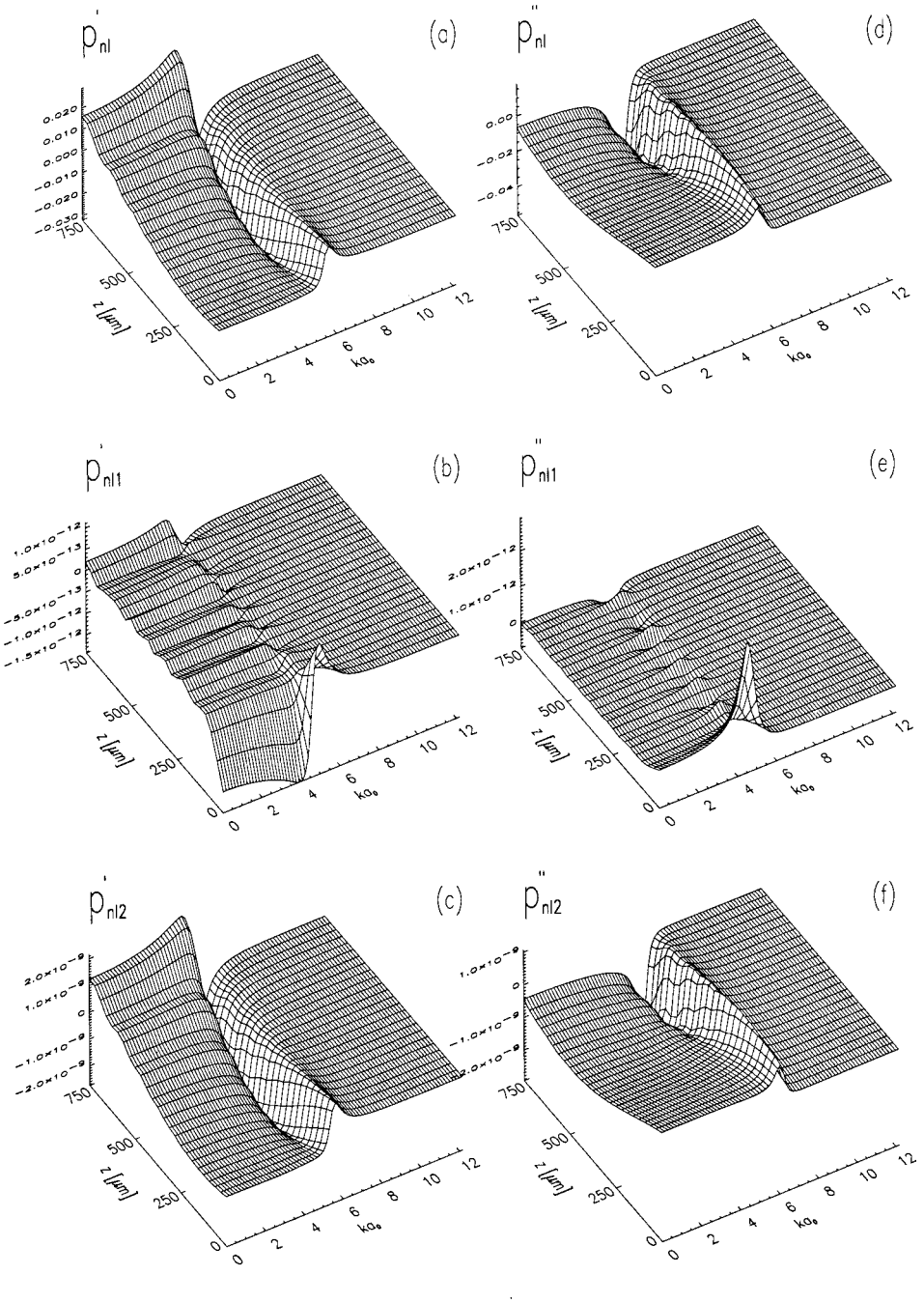

FIG. 4. Longitudinal dependence of the Wigner distribution of the real part of the nonlinear interband polarization $p'_{\mathrm{nl}}(k,z,t)$ (left column) and the imaginary part of the nonlinear interband polarization $p''_{\mathrm{nl}}(k,z,t)$ (right column). The pump beam (5 mW) and the probe beam (5 μW) are strongly detuned ($\delta\omega=3$ GHz).

shows a lower amplitude in both the real and imaginary parts, since the rather weak coupling of the pump-probe interaction keeps the amplitude of the conjugate wave at a strongly damped level. At the same time, the conjugate wave is spectrally situated within the absorption regime, efficiently preventing an induced change from absorption towards gain.

D. Oblique incidence

The spatiotemporally resolved calculation of the propagating fields in the active area allows one to investigate dynamic spatiospectral changes in the Wigner distributions that arise from different beam properties or injection conditions. Thus one can vary not only the power and wavelength of the pump and probe beam but also the beam width as well as injection angle and lateral position of injection, which in concert lead to different dynamic spatiospectral overlap during propagation. As an example, we will consider a situation where the pump beam propagates perpendicular to the front and back facets of the amplifier while the probe beam ($\omega=\omega-\delta\omega$, $\delta\omega=3$ GHz) is injected at an angle of $\alpha=25°$, 20 μm below the center of the amplifier. Due to the rather large spatial overlap of the two beams during their propagation (each having a beam waist of 50 μm), the longitudinal dependence of the Wigner distributions shows a qualitatively very similar behavior. In the following, we thus focus on the transverse dependence of the Wigner distribution of the interband polarization of the probe beam, p_{nl1}, displaying the distributions at three longitudinal positions. Figure 6 visualizes the real part, p'_{nl1}, in the left column [Figs. 6(a)–6(c)],

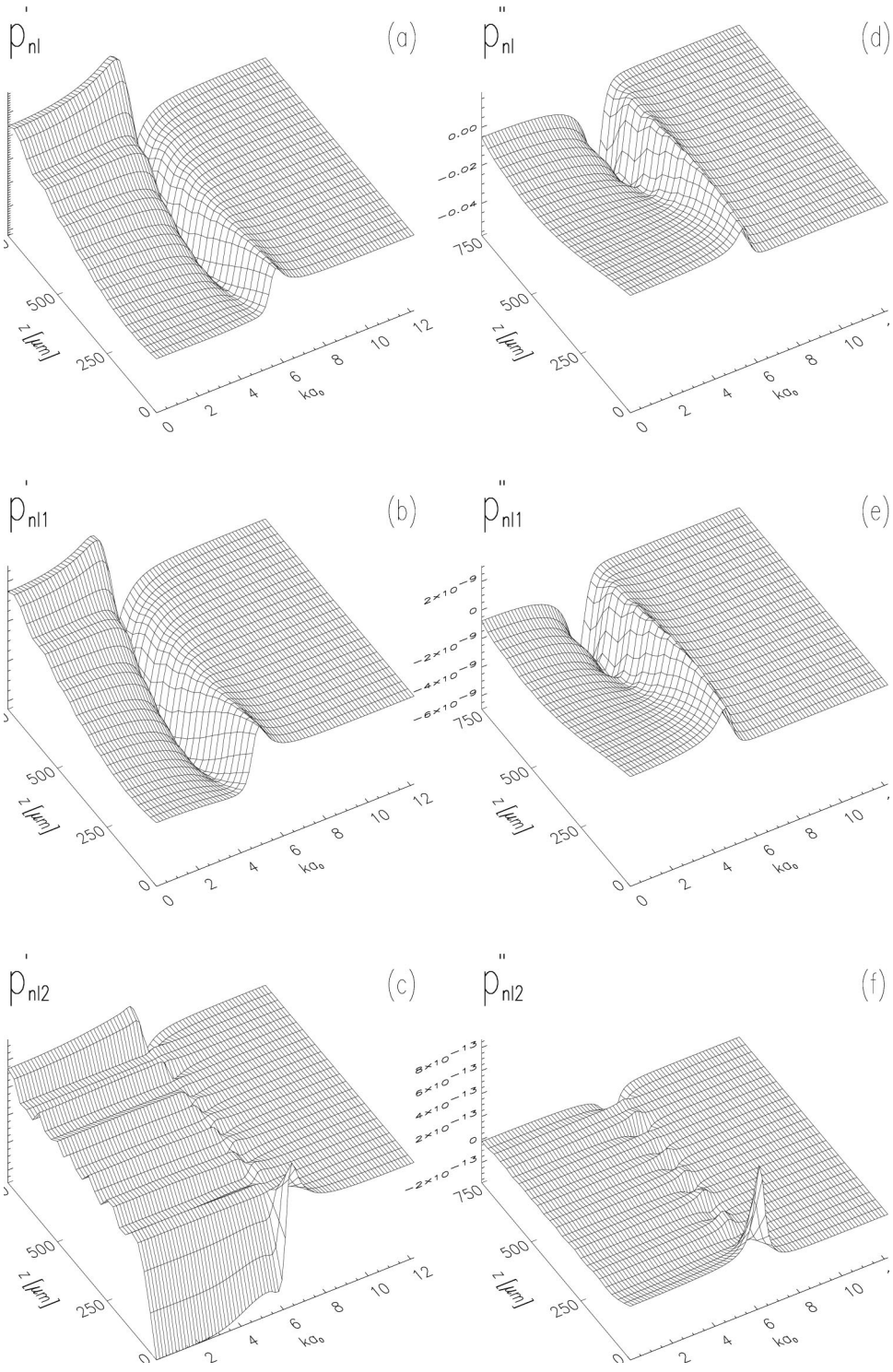

FIG. 5. Wigner distribution of the real part of the nonlinear interband polarization $p'_{\mathrm{nl}}(k,z,t)$ (left column) and the imaginary part of the nonlinear interband polarization $p''_{\mathrm{nl}}(k,z,t)$ (right column) for the situation of parallel injection of the pump beam (5 mW) and the probe beam (5 μW) of higher frequency at small detuning $\delta\omega = 100$ MHz.

and the imaginary part of the polarization of the probe beam, p'_{nl1} [Figs. 6(d)–6(f)], in the right column. Figures 6(a) and 6(d) shows typical snapshots at the front facet, at $z=0$, i.e., right after the optical injection. Due to the oblique incidence of the probe beam, a phase modulation can be observed in the lateral dependence. One can see from the amplitude of the distribution that the light field is injected laterally displaced with respect to the center of the facet. In the middle of the amplifier, at $z=L/2$, as displayed in Figs. 6(b) and 6(e), the probe light field has already propagated towards the center increasing the spatiospectral overlap with the pump beam. This is also verified in Figs. 6(c) and 6(f), in the real [Fig. 6(c)] and imaginary [Fig. 6(f)] part of the nonlinear interband polarization of the probe field. An interesting effect, which has already been observed in [20], is that the propagation of the probe beam inside the semiconductor plasma significantly deviates from the path projected by geometrical optics. The increased intersection area in Figs. 6(b) and 6(e) leads to a trapping of the weak probe beam caused by the spatio-spectral gain, thus staying more or less in its lateral position when advancing from the situation displayed in Figs. 6(b) and 6(e) to $z=L$ displayed Figs. 6(c) and 6(f).

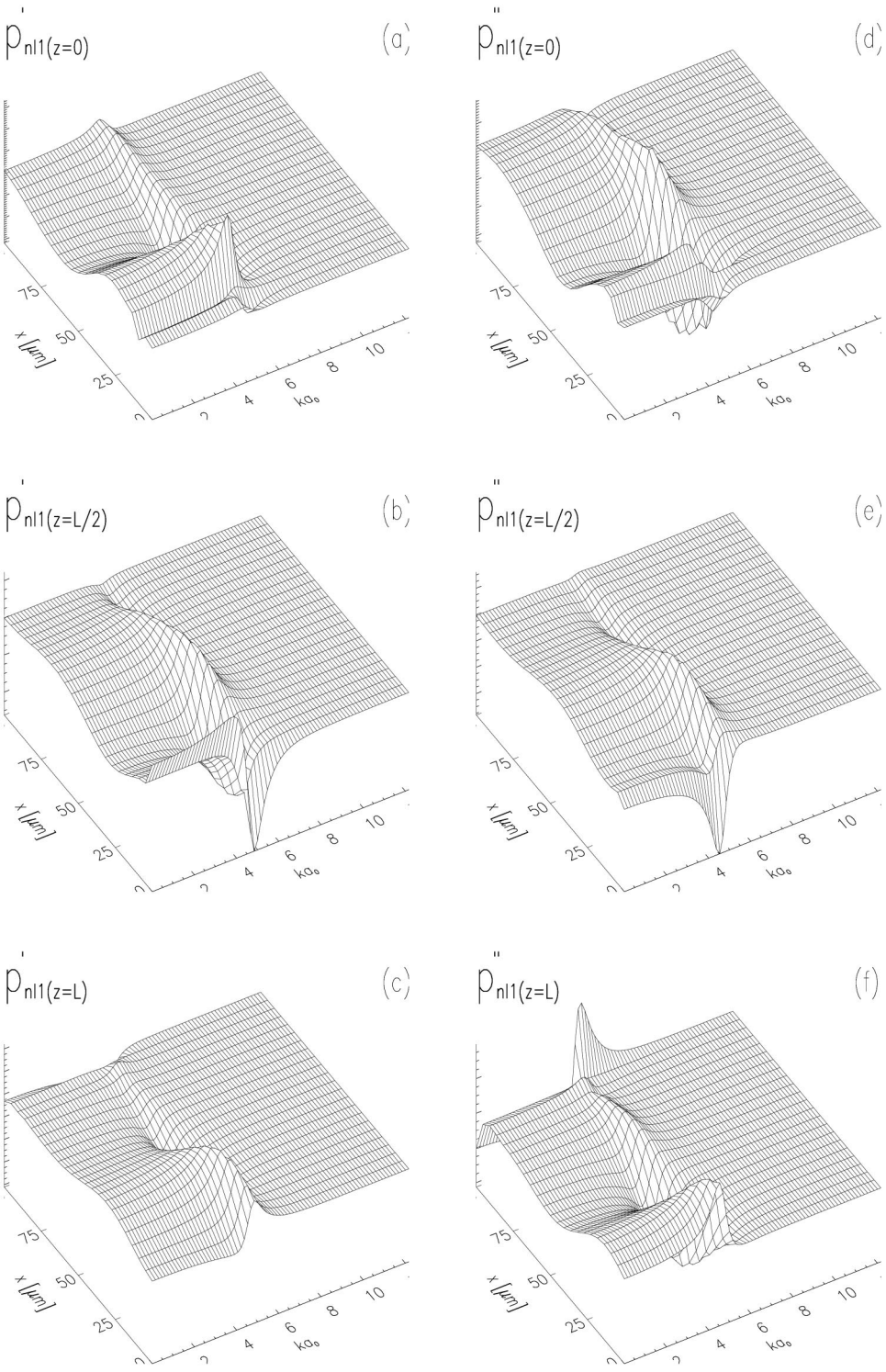

FIG. 6. Lateral cuts of the Wigner distributions of the real part of the nonlinear interband polarization $p'_{\mathrm{nl1}}(k,x,t)$ (left column) and the imaginary part of the nonlinear interband polarization $p''_{\mathrm{nl1}}(k,x,t)$ (right column) of the probe beam. The pump beam (5 mW) is propagating in a direction perpendicular to the facets of the amplifier facets and the probe beam (5 μW) is injected 20 μm below the middle of the facet at an injection angle of 25° with resepct to the surface normal.

IV. CONCLUSION

In conclusion, we have theoretically investigated the dynamic spatiospectral propagation and wave mixing of optical fields within the active area of a broad-area semiconductor laser. In a novel theoretical description of spatiospectral wave mixing based on Maxwell-Bloch equations for spatially inhomogeneous semiconductor lasers, we show that a microscopic treatment involving a third-order expansion in terms of the carrier distributions unites and bridges two previously distinct limits. This allows us to consistently include various relevant interactions and physical mechanisms with time constants ranging from the subpicosecond to the nanosecond regime. Those are, in particular, microscopic spatiospectral interactions of the light fields leading to gain nonlinearities and spatial and spectral hole burning as well as nonequilibrium dynamics of the carrier temperatures, carrier transport, population pulsations, optical self-focusing, and diffraction. It is the combined consideration of these effects within our microscopic treatment which allows an investigation of small (MHz) and large (GHz to THz) detunings as well as detunings in the intermediate regime (MHz to GHz) of the propagating light fields. It thus offers a new detailed analysis of wave-mixing phenomena in nonlinear media in

which the lateral and longitudinal dependence as well as counterpropagation effects are taken into account.

Results obtained from extensive numerical simulations demonstrate that the Wigner distributions of the electrons and the interband polarizations reveal—due to their simultaneous dependence on frequency, space, and time—the relevant spectral and spatial time scales involved in the carrier and light-field dynamics. In particular, they visualize dynamic spatiospectral carrier and energy transfer, mode competition within the bandwidth of the amplifier with its dependence on the detuning, spatiospectral hole burning, and induced gain and index variations. It could thus be demonstrated that in spatially inhomogeneous semiconductor media, those processes determine the spatial and spectral properties of the light fields along with their way of propagation. As a result, radiation may be guided or even trapped by the carrier plasma in the semiconductor medium.

Generally, the theoretical description may be applied, e.g., to spatiotemporal pump-probe situations with short optical pulses providing information of the temporal and spatial pulse shape, dynamic frequency changes, nonlinear spatiospectral gain saturation, or the investigation of material properties and calculation of relevant time scales. Thus our microscopic theory of dynamic spatiospectral wave mixing provides the basis for a theoretical description and analysis of a whole class of pump-probe experiments and allows an identification and quantification of the underlying physical interactions.

[1] H. Nakajima and R. Frey, IEEE J. Quantum Electron. **22**, 1349 (1986).
[2] R. Nietzke, P. Panknin, W. Elsässer, and E. O. Göbel, IEEE J. Quantum Electron. **25**, 1399 (1989).
[3] R. Nietzke, W. Elsässer, A. N. Baranov, and K. Wünstel, Appl. Phys. Lett. **58**, 554 (1991).
[4] S. Murata, A. Tomita, J. Shimiza, M. Kitamura, and A. Suzuki, Appl. Phys. Lett. **58**, 1458 (1991).
[5] S. R. Chinn, Appl. Phys. Lett. **59**, 1673 (1991).
[6] K. Kikuchi, M. Kakui, C.-E. Zah, and T.-P. Lee, IEEE J. Quantum Electron. **28**, 151 (1992).
[7] G. P. Agrawal, J. Opt. Soc. Am. B **5**, 147 (1987).
[8] M. Yamada, J. Appl. Phys. **66**, 81 (1989).
[9] W. M. Yee and K. A. Shore, J. Opt. Soc. Am. B **11**, 1221 (1994).
[10] U. Herzog, Opt. Commun. **82**, 390 (1991).
[11] A. Schulze, A. Knorr, and S. W. Koch, Phys. Rev. B **51**, 10 601 (1995).
[12] A. Girndt, A. Knorr, M. Hofmann, and S. W. Koch, J. Appl. Phys. **78**, 2946 (1995).
[13] A. Uskov, J. Mórk, and J. Mark, IEEE J. Quantum Electron. **30**, 1769 (1994).
[14] A. Mecozzi, A. D'Ottavi, and R. Hui, IEEE J. Quantum Electron. **29**, 1477 (1993).
[15] O. Hess and T. Kuhn, Phys. Rev. A **54**, 3360 (1996).
[16] E. Gehrig and O. Hess, Phys. Rev. A **57**, 2150 (1998).
[17] O. Hess and T. Kuhn, Phys. Rev. A **54**, 3347 (1996).
[18] M. Sargent III, F. Zhou, and S. W. Koch, Phys. Rev. A **38**, 4673 (1998).
[19] F. Zhou, M. Sargent III, and S. W. Koch, Phys. Rev. A **41**, 463 (1990).
[20] E. Gehrig and O. Hess, J. Opt. Soc. Am. B **15**, 2861 (1998).